

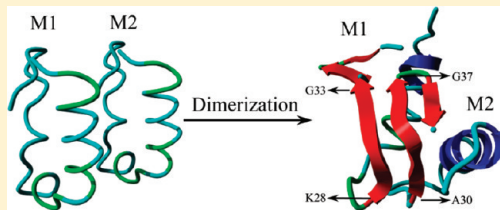
# Dimerization of the Full-Length Alzheimer Amyloid $\beta$ -Peptide ( $A\beta42$ ) in Explicit Aqueous Solution: A Molecular Dynamics Study

Xiaoxia Zhu, Ram Prasad Bora, Arghya Barman, Rajiv Singh, and Rajeev Prabhakar\*

Department of Chemistry, University of Miami, 1301 Memorial Drive, Coral Gables, Florida 33146, United States

## S Supporting Information

**ABSTRACT:** In this study, the mechanism of dimerization of the full-length Alzheimer amyloid beta ( $A\beta42$ ) peptide and structural properties of the three most stable dimers have been elucidated through  $0.8 \mu s$  classical molecular dynamics (MD) simulations. The  $A\beta42$  dimer has been reported to be the smallest neurotoxic species that adversely affects both memory and synaptic plasticity. On the basis of interactions between the distinct regions of the  $A\beta42$  monomer, 10 different starting configurations were developed from their native folded structures. However, only six of them were found to form dimers and among them the three most stable ( $X^P$ ,  $C-C^{AP}$ , and  $N-N^P$ ) were chosen for the detailed analysis. The structural properties of these dimers were compared with the available experimental and theoretical data. The MD simulations show that hydrophobic regions of both monomers play critical roles in the dimerization process. The high content of the  $\alpha$ -helical structure in all the dimers is in line with its experimentally proposed role in the oligomerization. The formation of a zipper-like structure in  $X^P$  is also in accordance with its existence in the aggregates of several short amyloidogenic peptides. The computed values of translational ( $D_T$ ) and rotational ( $D_R$ ) diffusion constants of  $0.63 \times 10^{-6} \text{ cm}^2/\text{s}$  and  $0.035 \text{ ns}^{-1}$ , respectively, for this dimer are supported by the corresponding values of the  $A\beta42$  monomer. These simulations have also elucidated several other key structural properties of these peptides. This information will be very useful to design small molecules for the inhibition and disruption of the critical  $A\beta42$  dimers.



## I. INTRODUCTION

Alzheimer's disease (AD) is a progressive neurodegenerative disorder that is characterized by the abnormal deposition of extracellular senile plaques and intracellular neurofibrillary tangles.<sup>1–3</sup> A wealth of genetic, animal modeling, and biochemical data indicates that amyloid  $\beta$  ( $A\beta$ ) peptide is the main component of these plaques.<sup>2,4–8</sup>  $A\beta$  is naturally derived in the brain through the proteolytic cleavage of amyloid precursor protein (APP) by  $\beta$ - and  $\gamma$ -secretase enzymes.<sup>9–11</sup> The two predominant forms of the  $A\beta$  peptides produced *in vivo* are 40–42 containing amino acid residues ( $A\beta40$  and  $A\beta42$ ), but only the latter has been observed to be a major contributor (ca. 90%) of the amyloid plaques.<sup>12–15</sup> A combination of size exclusion chromatography (SEC), quasi-elastic light scattering, electron microscopy, and imaging techniques demonstrated that in both AD and control brains the  $A\beta$ -peptide can self-associate to form several different assembly forms, from dimers all the way to aggregates of amyloid fibrils.<sup>16–22</sup> All distinct assembly forms of  $A\beta$  have been found to be neurotoxic, but the extent and mechanism of toxicity differed.<sup>23</sup> The  $A\beta$  dimers isolated from neuritic and vascular amyloid deposits have been shown to be more toxic to neurons in the presence of microglia.<sup>24</sup> Recently, they have also been extracted directly from the Alzheimer's brains and reported to be the smallest synaptotoxic species that impair synaptic plasticity and memory.<sup>25</sup> In addition, Walsh et al. have shown the potential synaptotoxicity of  $A\beta$  dimer *in vivo*.<sup>26</sup>

The fluorescence resonance energy transfer experiments showed that  $A\beta42$  forms stable dimers in solution.<sup>27–29</sup> However, due to the fast rate of aggregation, a high resolution structural determination of these early  $A\beta$  aggregates through experimental techniques is extremely difficult.<sup>30–32</sup> In this aspect, molecular dynamics (MD) simulations provide a very useful tool to derive valuable information regarding the secondary structures of the  $A\beta$  peptides. In the past few years, a variety of simulation techniques from coarse grained to the all-atom with implicit and/or explicit solvent models have been successfully applied to investigate the structures and dynamics of the selected small fragments<sup>33–44</sup> and full-length  $A\beta$  dimers.<sup>45–47</sup> A recent MD simulation study on the formation of the  $A\beta(1–39)$  dimer using the implicit solvent model showed the dominant parallel N-terminus conformations and salt-bridges between Lys28 of one chain and either Glu22 or Asp23 of the other chain.<sup>37</sup> Karplus and co-workers performed MD simulations to investigate the dimerization of  $A\beta(16–22)$  peptide and its mutant forms and showed that the dimers exhibited all possible combinations of  $\beta$ -sheets with an overall preference for antiparallel arrangements.<sup>38</sup> García et al. also performed replica exchange molecular dynamics (REMD) simulations on the dimer of the same peptide and suggested the formation of six different stable dimers that are not only limited

Received: October 18, 2011

Revised: March 23, 2012

Published: March 26, 2012

to parallel and antiparallel orientations.<sup>41</sup> They also proposed that water molecules are involved in stabilizing some dimer conformations. Itoh et al. studied the dimerization of the A $\beta$ (29–42) sequence using a multicanonical-multioverlap molecular dynamics simulation and showed conformational changes from helical to strand structures step by step.<sup>39</sup> The discrete molecular dynamics (DMD) simulations on coarse-grained models of the full-length A $\beta$ 42 indicated that dimer conformations have higher free energies compared to their corresponding monomeric states.<sup>42</sup> These studies have provided valuable insights into the structures and stabilities of dimers of different A $\beta$  fragments. However, the nature and conformation of a peptide in solution depends upon its length and specific amino acid residue sequence. For instance, A $\beta$ 40 and A $\beta$ 42 differ only by two C-terminal hydrophobic residues (Ile and Ala), but they follow distinct aggregation mechanisms and form fibrils with different morphologies.<sup>30,48–50</sup> Therefore, the dimeric structures of the full-length A $\beta$ 42 peptide in explicit solvent are required for a deeper understanding of their structural properties.

A large number of studies suggest that three distinct regions of the A $\beta$  monomer, the central hydrophobic core (CHC, Leu17-Ala21), a turn region (TR, Val24-Asn27), and the second hydrophobic region (SHR, Gly29-Met35), play important roles in the aggregation process.<sup>51–54</sup> The hydrophobic interactions between these regions of the monomers provide the required driving/stabilizing force for A $\beta$  oligomerization, and they undergo substantial structural reorganization during the process.<sup>55–59</sup> In addition, the charged residues present in the peptide have been reported to influence both the dynamics of aggregation and stability of  $\beta$ -sheets.<sup>51,52,54,60–65</sup> For instance, the solid state NMR (ssNMR) data on amyloid fibrils showed that the Glu22/Asp23 and Lys28 residues form both intra- and interchain salt-bridges.<sup>51,52,54,66</sup> Recently Petkova et al. reported the formation of amyloid fibrils with distinctive morphologies and toxicities and suggested that oligomerization may proceed through different pathways during the fibril growth.<sup>54</sup>

The models of the A $\beta$ 42 dimer for MD simulations can be developed using the following two approaches: (1) top down and (2) bottom up. In the “top down” approach, the starting structure of dimer is derived from a structure of high order ( $n$ ) oligomer by removing  $n - 2$  monomers. However, here the initial structures of both monomers are already unfolded and rich in  $\beta$ -sheet characters which do not resemble their native hairpin-like conformations.<sup>40,42</sup> On the other hand, the “bottom up” approach can accurately simulate the actual dimerization process starting from the native folded structures of the monomers.

In the present study, we have applied the “bottom up” approach to build models of the full-length A $\beta$ 42 dimers for all-atom classical MD simulations in explicit aqueous solution. On the basis of interactions between different regions (N-terminus, CHC, TR, SHR, and C-terminus) of the two A $\beta$ 42 monomers, 10 different starting structures have been used in 0.8  $\mu$ s long simulations. These simulations will provide both the mechanism of dimerization and structures of different dimers which will help to elucidate roles of specific regions of the peptide in this process. The structural features of these dimers are compared with the available experimental and theoretical information. The relative stability of the different dimers is determined by comparing their electrostatic binding energies. The most stable dimer is further used to compute the

translational diffusion constant ( $D_T$ ) and rotational diffusion constant ( $D_R$ ). These parameters could be measured by pulse field gradient (PFG)-NMR and dynamic light scattering (DLS) experiments.<sup>67–70</sup> The results reported in this study will provide a deeper understanding of the dimerization process and advance our efforts to design small molecules for the inhibition and disruption of the A $\beta$ 42 dimers.

## II. COMPUTATIONAL PROCEDURE

**Ila. MD Simulations.** All MD simulations were performed using the GROMACS program<sup>71–73</sup> utilizing the GROMOS force field 53AS.<sup>73</sup> This force field has previously been successfully employed to predict the structures of the A $\beta$  peptides<sup>33,42,44–46</sup> and other biomolecules.<sup>74–77</sup> The solvent molecules were modeled with the simple point charge (SPC) water model.<sup>78</sup> For all simulations, the starting structures were immersed in a cubic box with a buffer of 2.0 nm between the peptide and the edge of the box. This ruled out unwanted effects that may arise from the applied periodic boundary conditions (PBC). Some water molecules were replaced by sodium and chloride ions to neutralize the system. The starting structures were subsequently energy-minimized with a steepest descent method for 3000 steps. The resulting minimized structures are utilized as the initial structures for the MD simulations. The MD simulations were performed in the following two steps: (1) equilibration of the initial structures for 50 ns in a time period called the equilibration phase, and (2) the most representative structures obtained during the 50 ns equilibration period are further simulated for an additional 50 ns in a time period described as the production phase. The MD simulations were carried out under the NPT ensemble conditions. The SETTLE algorithm was used to constrain the bond lengths and the angles of the water molecules,<sup>79</sup> whereas the LINCS algorithm was used to constrain the bond length of the peptides.<sup>80</sup> The long-range electrostatic interactions were calculated by the particle-mesh Ewald method.<sup>81,82</sup> Peptide, water molecules, and ions were coupled separately to a bath at 300 K with a coupling constant of 0.1 ps.

The tools available in the GROMACS program package and the YASARA program have been utilized to analyze the different MD trajectories.<sup>83</sup> The secondary-structure analyses were performed by employing the defined secondary structures of proteins (DSSP) protocol.<sup>84</sup> In the analysis, the starting structure of the production phase (the most representative structure during the 50 ns equilibration phase) was utilized as the reference structure. The contact maps for the most representative structures obtained from a cluster analysis have also been employed as structural descriptors. A contact for a pair of amino acid side chains is considered to be formed when a minimal distance between any pair of their atoms is less than 0.5 nm. In the cluster analysis, the trajectories are analyzed by grouping structurally similar frames (root-mean-square deviation cutoff = 0.3 nm),<sup>85</sup> and the frame with the largest number of neighbors is denoted as a middle structure, which represents that particular cluster.

**Ilb. Computational Models.** The most representative structure derived from the previous 50 ns all-atom MD simulation<sup>86</sup> on the full-length A $\beta$ 42 monomer structure (model 10 of PDB: 1IYT<sup>87</sup>) was used to develop all the starting configurations. This structure has been utilized as a starting point in several recent MD studies,<sup>88–90</sup> and the equilibrated structure provided by the simulations reproduced several key experimental features.<sup>86</sup> On the basis of interactions

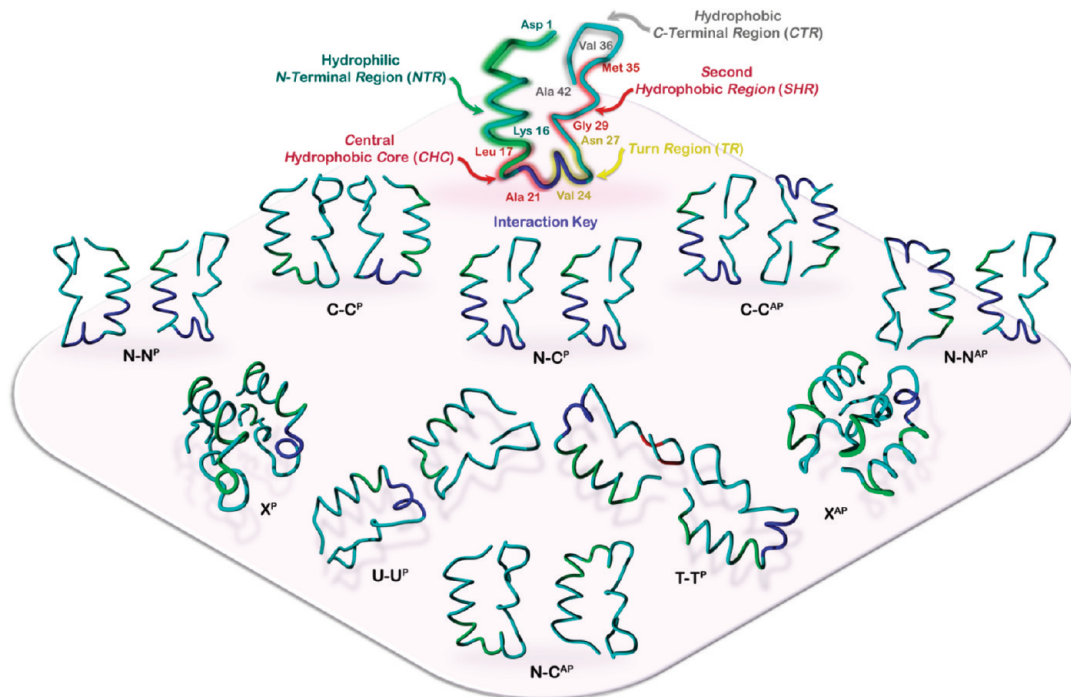


**Figure 1.** Ten different starting geometries for MD simulations.

between different regions (N-terminus, CHC, TR, SHR, and C-terminus) of the two  $\text{A}\beta 42$  monomers (M1 and M2), the following 10 different starting structures have been used (Figure 1): (1) the parallel N-termini and CHC regions of M1 and M2 ( $\text{N}-\text{N}^{\text{P}}$ ); (2) the parallel C-termini and SHR segments of M1 and M2 ( $\text{C}-\text{C}^{\text{P}}$ ); (3) the N-terminus of M1 is parallel to the C-terminus of M2 ( $\text{N}-\text{C}^{\text{P}}$ ); (4) the helix-loop-strand (HLS) regions of M1 and M2 are parallel to each other ( $\text{X}^{\text{P}}$ ); (5) the antiparallel N-termini and CHC regions of M1 and M2 ( $\text{N}-\text{N}^{\text{AP}}$ ); (6) the antiparallel C-termini and SHR segments of M1 and M2 ( $\text{C}-\text{C}^{\text{AP}}$ ); (7) the N-terminus of M1 is antiparallel to the C-terminus of M2 ( $\text{N}-\text{C}^{\text{AP}}$ ); (8) the helix-loop-strand (HLS) regions of M1 and M2 are antiparallel to each other ( $\text{X}^{\text{AP}}$ ); (9) the parallel TR segments of M1 and M2 ( $\text{U}-\text{U}^{\text{P}}$ ); and (10) the parallel tails of the N- and C-terminus of M1 and M2, respectively ( $\text{T}-\text{T}^{\text{P}}$ ). In these configurations, the initial separation between the center of mass of each monomer was kept at 25 Å to allow them sufficient space for tumbling. The minimum distance between the two monomers was 5 Å. This also ruled out any bias in their initial configurations, such as intermolecular interactions and preformation of a salt-bridge between two monomers. In order to investigate the effects of the starting structure and force field, dimerization of the most stable dimer was also studied using a different  $\text{A}\beta 42$  monomer structure (PDB: 1Z0Q<sup>91</sup>) and OPLS (optimized potential for liquid simulations) force field<sup>92,93</sup> using the TIP3P water model<sup>94</sup> through exactly the same procedure.

**IIC. Solvation Energy Calculation.** The solvation energy ( $\Delta G_{\text{sol}}$ ) was computed using the following equation.

$$\Delta G_{\text{sol}} = \Delta G_{\text{binding}}^{\text{ele}} + \Delta G_{\text{binding}}^{\text{nonpolar}}$$

where  $\Delta G_{\text{binding}}^{\text{ele}}$  and  $\Delta G_{\text{binding}}^{\text{nonpolar}}$  represent the electrostatic and nonpolar contributions to the solvation energy, respectively. In order to compute electrostatic interactions between monomers, a continuum electrostatic calculation was performed using the APBS software.<sup>95,96</sup> The relative electrostatic binding energies

between the two  $\text{A}\beta 42$  monomers (M1 and M2) were calculated using the following equation:

$$\Delta G_{\text{binding}}^{\text{ele}} = \Delta G_{\text{desol}_M1}^{\text{ele}} + \Delta G_{\text{desol}_M2}^{\text{ele}} + E_{M1-M2}^{\text{ele}}$$

where  $\Delta G_{\text{desol}_M1}^{\text{ele}}$  describes the desolvation energy of M1 after its binding with M2. Due to the association between M1 and M2, the former loses the electrostatic interactions with solvent. The following two-step procedure was used to calculate this energy: (1) calculation of the electrostatic energy between M1 and the surrounding solvent in the absence of M2 and (2) computation of the electrostatic energy of M1 with the surrounding solvent in the presence of M2 (provided M2 does not carry any partial charge).<sup>97</sup> The difference in energies calculated in these two steps will provide the electrostatic desolvation energy  $\Delta G_{\text{desol}_M1}^{\text{ele}}$  or  $\Delta G_{\text{desol}_M2}^{\text{ele}}$ . The last term in the equation describing electrostatic interaction ( $E_{M1-M2}^{\text{ele}}$ ) was computed using the electrostatic potential ( $\varphi_i$ ) generated by M1 at the position of the atomic charges ( $q_i$ ) of M2 by solving the following equation.

$$E_{M1-M2}^{\text{ele}} = \sum_i^N \varphi_i q_i$$

The complexation of two monomers (M1 and M2) was computed by solving the Poisson–Boltzmann equation. These calculations were performed at room temperature (298.15 K) using dielectric constants of 2.0 and 78.0 for protein and water environments, respectively, and the probe sphere of 1.5 Å radius was used for calculating the solute surface. The grid spacing was set to 0.35 Å, and the dielectric boundary was defined as the van der Waals surface. The salt concentration of 50 mM was used for the calculation. For these calculations, all the structures in the PDB format were converted to the PQR format using the PDB2PQR server.<sup>98,99</sup> The nonpolar contribution to free energy is computed from the burial of

solvent accessible surface area (SASA) of the peptides upon binding using the following equation.

$$\Delta G_{\text{binding}}^{\text{nonpolar}} = \gamma \times \text{SASA}$$

where SASA values of the individual monomer and dimer complexes are calculated utilizing the YASARA program.<sup>83</sup> The microscopic surface tension coefficient ( $\gamma = 0.00542 \text{ kcal/mol} \text{ Å}^2$ ) connects the solvent accessible surface area to the free energy of transferring a molecule from alkane to water.<sup>100,101</sup>

### III. RESULTS AND DISCUSSION

In the present study, 0.8  $\mu\text{s}$  all-atom MD simulations in explicit water solvent are performed to investigate the dimerization of the full-length  $\text{A}\beta42$  peptide. As discussed in the Computational Models section, based on the interactions between different regions (N-terminus, CHC, TR, SHR, and C-terminus) of the two  $\text{A}\beta42$  monomers (M1 and M2), the following 10 different starting structures have been used (Figure 1): N–N<sup>P</sup>, C–C<sup>P</sup>, N–C<sup>P</sup>, X<sup>P</sup>, N–N<sup>AP</sup>, C–C<sup>AP</sup>, N–C<sup>AP</sup>, X<sup>AP</sup>, U–U<sup>P</sup>, and T–T<sup>P</sup>. After the first 50 ns simulations, 6 out of the 10 starting configurations (N–N<sup>P</sup>, X<sup>P</sup>, X<sup>AP</sup>, C–C<sup>AP</sup>, N–N<sup>AP</sup>, and N–C<sup>AP</sup>) were found to form dimeric structures, while the remaining four monomers drifted apart from each other and were found to possess no intermolecular interactions. All six dimers were further simulated for 50 ns (production phase simulations), which were used for detailed analysis. All of these structures were found to be well equilibrated only after the first 20 ns of the simulations in the production phase (Figure S1, Supporting Information).

During the simulations, both M1 and M2 monomers of all six dimers substantially lose their random coil conformation and acquire dominant helical conformation (Table 1). This increase

lowest for the X<sup>P</sup> dimer ( $-7.7 \text{ kcal/mol}$ ), and the energies of the other dimers are higher, i.e., C–C<sup>AP</sup> ( $-2.4 \text{ kcal/mol}$ ), N–N<sup>P</sup> ( $-0.4 \text{ kcal/mol}$ ), N–C<sup>AP</sup> ( $1.65 \text{ kcal/mol}$ ), X<sup>AP</sup> ( $2.0 \text{ kcal/mol}$ ), and N–N<sup>AP</sup> ( $5.2 \text{ kcal/mol}$ ). The inclusion of the hydrophobic binding energy in these calculations retains X<sup>P</sup>, C–C<sup>AP</sup>, and N–N<sup>P</sup> as the three most stable dimers. It further increases the relative stability of X<sup>P</sup> ( $-16.3 \text{ kcal/mol}$ ) and provides N–N<sup>P</sup> ( $-7.7 \text{ kcal/mol}$ ) and C–C<sup>AP</sup> ( $-7.6 \text{ kcal/mol}$ ) as the two next isoenergetic aggregates (Table 2). On the basis of the energies, the structural characteristics of only these dimers will be discussed in detail in the next section. Since X<sup>P</sup> was found to be the most stable dimer, it was used as the model to compute translational ( $D_T$ ) and rotational ( $D_R$ ) diffusion constants.

**IIIa. Structural Features of the X<sup>P</sup> Dimer.** In the starting structure of this dimer, all three specific regions (CHC, TR, and SHR) of M1 and M2 were parallel to each other (Figure 1). During the simulation, the dimerization is driven by the formation of several hydrophobic, salt-bridge and hydrogen bonding interactions. The most representative structure derived from the X<sup>P</sup> simulation is shown in Figure 2a. In this structure, the C-terminal regions of M1 and M2 are stabilized by intermolecular parallel  $\beta$ -sheet structures. The contact map of this simulation shows a large cluster of contacts between the CHC–CHC and SHR–SHR regions of both monomers (Figure 2b). The N-terminal and CHC regions interact with each other through hydrophobic interactions between Gln15, Lys16, Phe19, and Phe20 of M1 and His13, Leu17, and Ala21 of M2. The Lys28–Ala33 region of M1 forms a zipper-like structure through hydrogen bonds with the Ala30–Gly37 segment of M2. The time dependent variation of the inter- and intramolecular  $\beta$ -sheet structure between the Gly25–Ala42 segments of M1 and Gly29–Ala42 of M2 shows a gradual growth of this conformation (Figure S2, Supporting Information). The GxxG motifs in the Gly25–Gly37 region have been proposed to have a major impact on  $\text{A}\beta42$  aggregation, which form a “glycine zipper”.<sup>103–105</sup> This zipper formation has also been experimentally proposed in aggregation of several amyloidogenic peptides.<sup>38,106</sup> In addition, the Lys28, Ala30, and Ile32 residues in the SHR region of M1 associate via hydrophobic interactions with Ile32, Met35, and Gly37 in the SHR segment of M2, respectively. Previous experimental studies also implicate this region in the oligomerization of the  $\text{A}\beta$  peptides.<sup>107,108</sup> Due to a large number of interactions, this structure contains the highest percentage of the  $\beta$ -sheet character (26.2%) among all dimers (Table 1).

Throughout the simulation, the CHC, TR, and SHR regions of both monomers largely retain their secondary structures (Figure 2c). However, they are quite flexible and the rmsd for M1 is found to be relatively smaller than the one for M2 (Figure S3a, Supporting Information). Among these regions, the TR fragment appears to be the most flexible. In M1, for the

**Table 1. Secondary Structure Compositions of Initial Monomer and Six Dimers**

alignment	helix	strand	turn	coil
A $\beta$ 42 monomer	14.3%	11.9%	23.8%	50.0%
N–N <sup>P</sup>	22.6%	16.7%	14.3%	46.4%
X <sup>P</sup>	22.6%	26.2%	13.1%	38.1%
X <sup>AP</sup>	31.0%	10.7%	11.9%	46.4%
C–C <sup>AP</sup>	26.2%	17.9%	14.3%	41.7%
N–N <sup>AP</sup>	39.3%	13.1%	4.8%	42.9%
N–C <sup>AP</sup>	29.8%	15.5%	9.5%	45.2%

in the helical character is consistent with the earlier observation that the assembly of  $\alpha$ -helices is a key step in the  $\text{A}\beta$  aggregation.<sup>102</sup> There is also a substantial enhancement in the beta-sheet content for the N–N<sup>P</sup>, X<sup>P</sup>, C–C<sup>AP</sup>, and N–C<sup>AP</sup> dimers (Table 1). The relative stabilities of these six dimers were determined by comparing their electrostatic binding energies (Table 2). The binding energy was found to be the

**Table 2. Solvation Free Energies of Six Dimers**

alignment	$E_{\text{elec}}$ (kcal/mol)	$\Delta G_{\text{sol\_A}}$ (kcal/mol)	$\Delta G_{\text{sol\_B}}$ (kcal/mol)	$\Delta G_{\text{elec}}$ (kcal/mol)	$\Delta G_{\text{nonpolar}}$ (kcal/mol)	$\Delta G_{\text{sol}}$ (kcal/mol)
N–N <sup>P</sup>	-11.5	5.9	5.2	-0.4	-7.3	-7.7
X <sup>P</sup>	-39.2	14.6	16.9	-7.7	-8.5	-16.3
X <sup>AP</sup>	-10.3	5.6	6.8	2.0	-9.1	-7.1
C–C <sup>AP</sup>	-15.0	6.8	5.7	-2.4	-5.3	-7.6
N–N <sup>AP</sup>	-5.0	5.8	4.4	5.2	-5.8	-0.6
N–C <sup>AP</sup>	-2.1	1.0	2.7	1.7	-4.1	-2.4

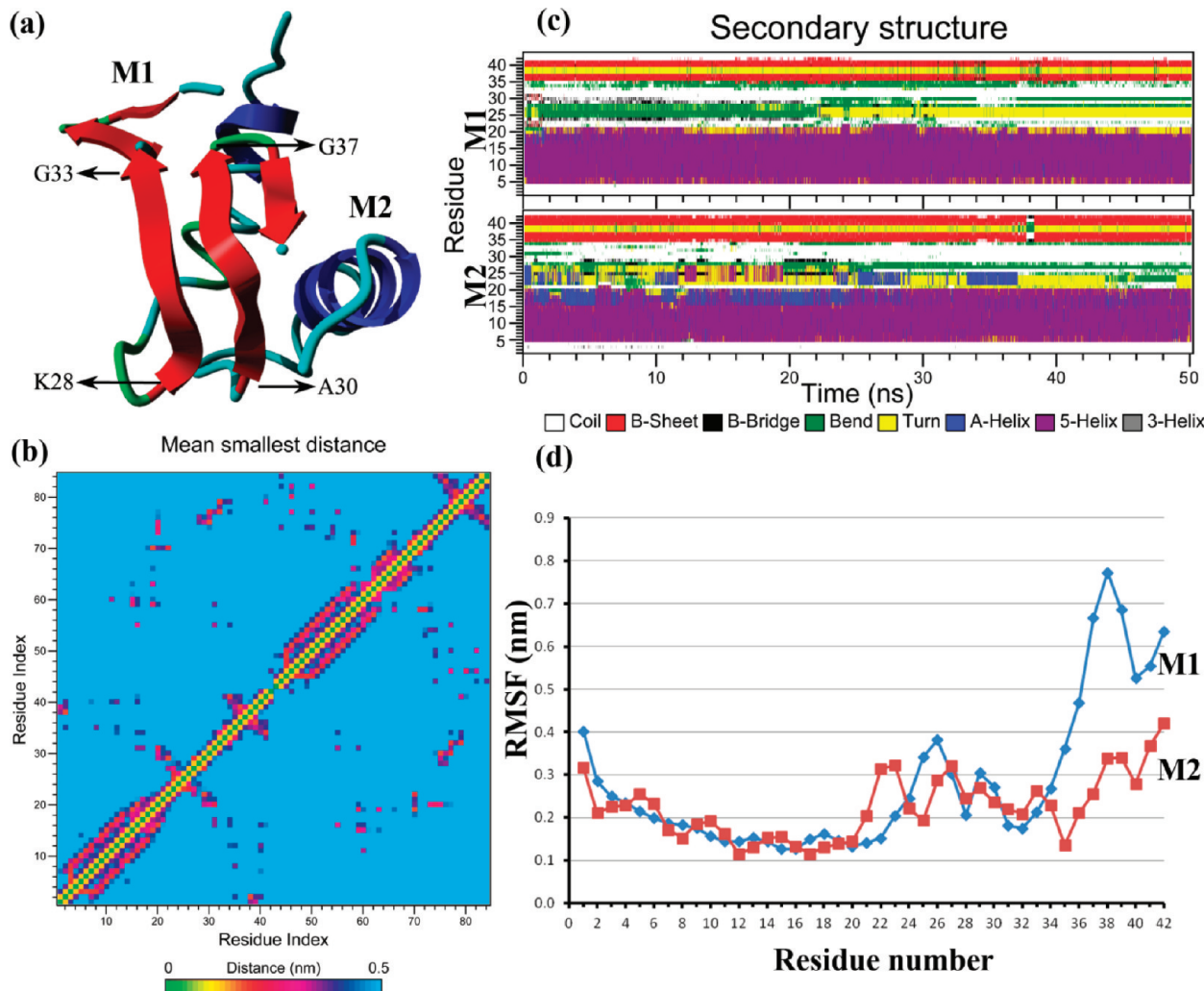


**Figure 2.** (a) Cartoon presentation of the most representative structure obtained by cluster analysis performed on 50 ns simulation in the production phase. (b) Contact map, where each square provides the mean average distance (intensity coded) of heavy atoms for the side chains of the residues which are less than 0.5 nm apart. (c) Secondary structure assignment per residue plotted against time. (d) Root-mean-square fluctuations (RMSF) of C<sub>α</sub> atoms of individual residues from each monomer of X<sup>P</sup> dimer.

first 22 ns, this region adopts the bend structure and then transforms into the turn conformation for the rest of the simulation (Figure 2c). An n-turn at residue *i* is assigned if there is a hydrogen bond from CO (*i*) to NH (*i* + *n*), i.e., n-turn (*i*) = H bond (*i*, *i* + *n*), *n* = 3, 4, 5. However, a bend is a structure with high curvature (>70°) that does not involve hydrogen bonds. However, in M2, it randomly switches between the turn, bend, α-helix, and random coil conformations. The SHR of M1 forms the bend and random coil structures, while in M2 it retains the random coil conformation. The atomic positional fluctuations of the C<sub>α</sub> atoms of each residue are shown in Figure 2d. This information is complementary to the aforementioned structural transformations and rmsd variations. The maximum fluctuations among the three critical regions in M1 and M2 are observed in the C-terminal region, with M1 being the most flexible. The relative stability of the C-terminus of M2 could be due to the greater β-sheet character and a large number of intramolecular hydrogen bond interactions with SHR. In both monomers, the minimum fluctuations are observed in the CHC region. This is due to stabilization provided by several hydrogen bonds and hydrophobic interactions between the CHC regions of the

monomers. These fluctuations are much smaller than the one observed in the monomer (Figure S4, Supporting Information). The time dependent variation of distance between Glu22 of M1 and Lys28 of M2 explicitly indicates the formation of a salt-bridge (Figure S5a, Supporting Information). This salt-bridge has been suggested to contribute to the kinetic barrier for aggregation in a previous MD study on the Aβ(1–39) dimer.<sup>37</sup> The ssNMR experiments also implicated this salt-bridge in the growth of oligomers.<sup>66</sup>

To test the dependence of the starting structure and force field parameters on the dimerization process, the aggregation of Aβ42 has been tested using another full-length Aβ42 monomer (PDB: 1Z0Q,<sup>91</sup> Figure S6, Supporting Information) and two different force fields (GROMOS and OPLS). The most representative structure (X<sup>P-1Z</sup>) derived from the production phase of the simulation using the GROMOS force field on the 1Z0Q structure is quite similar to X<sup>P</sup> (Figure S7, Supporting Information). For instance, in both structures (X<sup>P</sup> and X<sup>P-1Z</sup>), the Asn27-Gly33 and Leu34-Gly38 regions of M2 were found to form an intramolecular antiparallel β-sheet with each other and the latter also interacted with the Gly29-Gly33 segment of M1 through the intermolecular antiparallel β-sheet (Figure S7,

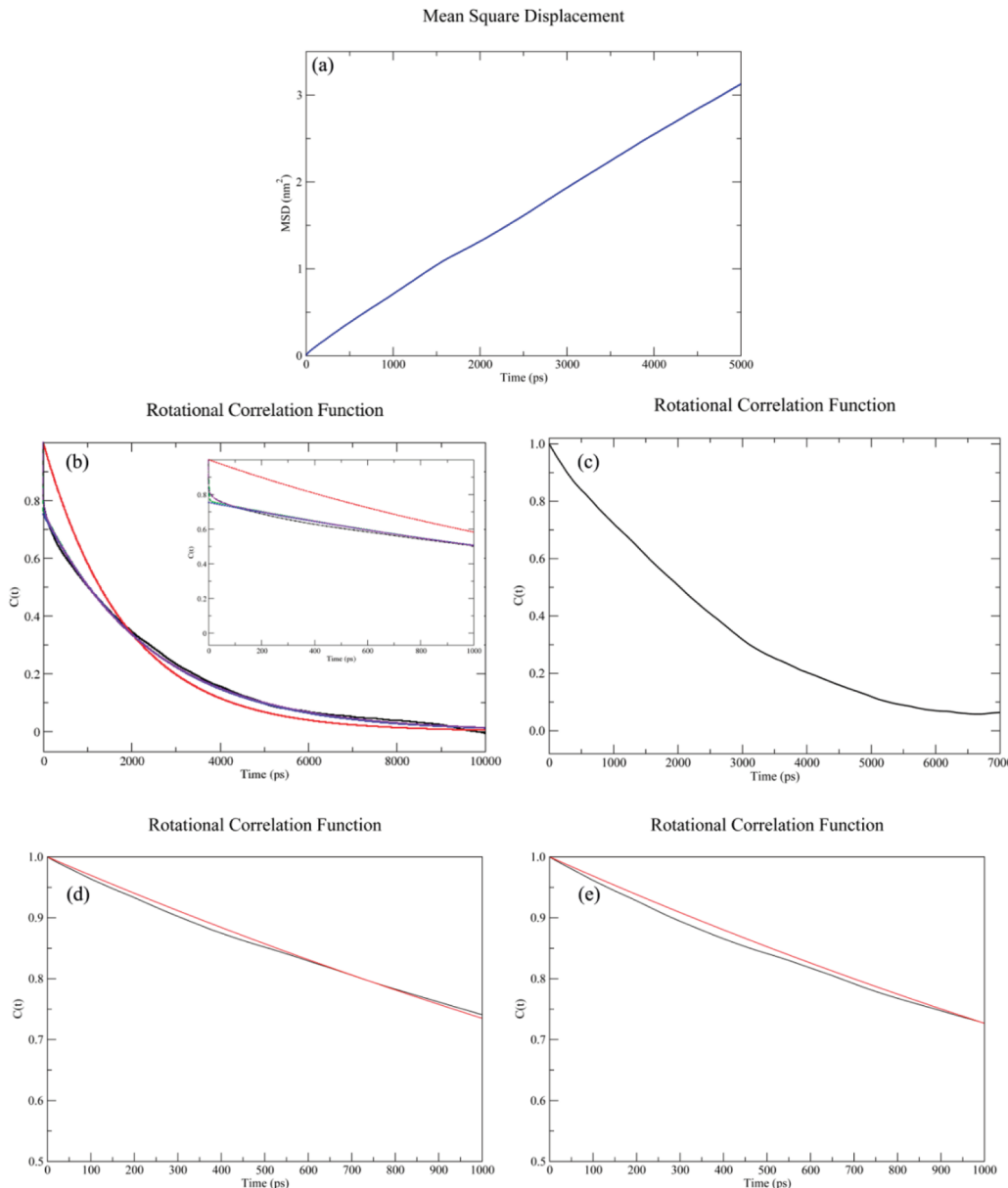


**Figure 3.** (a) The MSD of the center of mass of  $X^P$  dimer. (b) The total average correlation function  $C_{\text{tot}}^{\text{ave}}(t)$  derived from the first 10 ns MD simulation along with the model fitted functions, and the inset shows the first 1 ns behavior. (c) The total average rotational function  $C_{\text{rot}}^{\text{ave}}(t)$  generated using the procedure outlined in our previous paper. (d) The individual rotational correlation function  $C_{\text{rot}}(t)$  of the N–H backbone bond vector along with the fitted functions using eq 2 in the Supporting Information of Lys28 and (e) Ile32 amino acids.

Supporting Information). However, in comparison to  $X^P$ ,  $X^{P-1Z}$  contains a 7.2% lower  $\beta$ -sheet character (19%) and the intermolecular salt-bridge Glu22(M1)-Lys28(M2) is also broken in this structure. These results suggest that the aggregation of two different types of monomers with the same starting conformation and force field lead to the formation of the analogous dimeric structures with an overall structural similarity.

On the other hand, the effect of the OPLS force field on the dimerization was studied using the two different starting structures: (1) initial configuration used in the equilibration phase of the  $X^P$  simulation and (2) the most representative structure derived from the  $X^P$  simulation. The most representative structure ( $X^{P-O1}$ ) derived in the first case is very different from  $X^P$  (rmsd = 9.03 Å), Figure 2a and Figure S8 in the Supporting Information. The intermolecular  $\beta$ -sheet

(Lys28-Ala33 (M1)–Ala30-Gly37 (M2)) observed in  $X^P$  is completely lost in the  $X^{P-O1}$  dimer (Figure S8, Supporting Information). In addition, the secondary structure compositions of these dimers are also significantly different. The contents of both the  $\alpha$ -helix and  $\beta$ -sheet in  $X^{P-O1}$  are 15.5 and 21.4% lower than the corresponding values in  $X^P$  (Table 1). However, the coil character in  $X^{P-O1}$  is 23.8% greater than the one computed for  $X^P$ . In contrast to  $X^P$ , the Glu22(M1)-Lys28(M2) salt-bridge is also destroyed in this structure. These results indicate that the structures of  $\text{A}\beta 42$  dimers are sensitive to the nature of the force field. This observation is also supported by the large differences in the structures of  $\text{A}\beta 42$  monomers obtained using REMD simulations with OPLS<sup>109</sup> and ff99SB<sup>110</sup> force fields. However, among  $X^P$  and  $X^{P-O1}$ , the former was found to best reproduce the experimentally known features.<sup>106</sup>

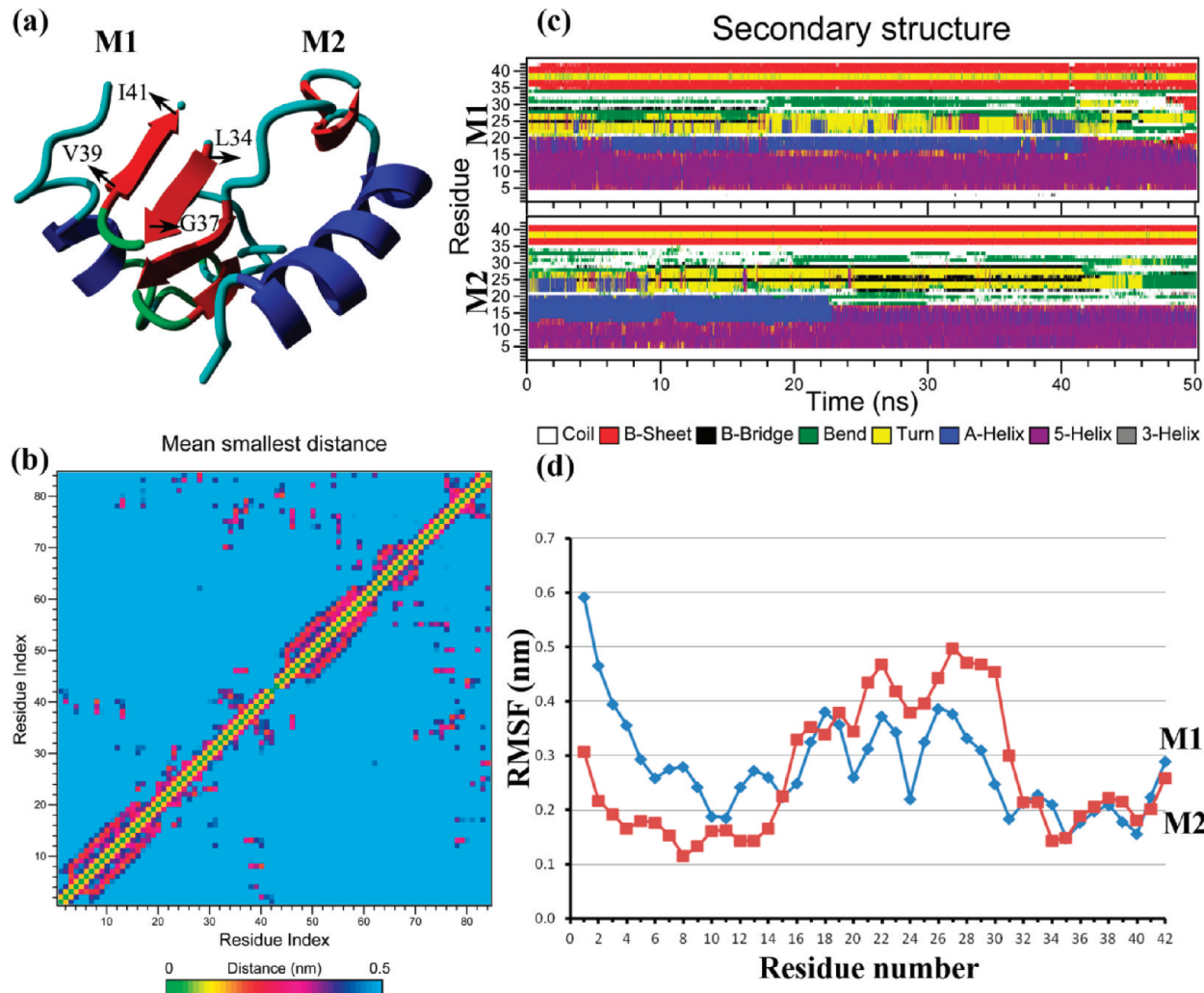


**Figure 4.** (a) Cartoon presentation of the most representative structure obtained by cluster analysis performed on 50 ns simulation in the production phase. (b) Contact map, where each square provides the mean average distance (intensity coded) of heavy atoms for the side chains of the residues which are less than 0.5 nm apart. (c) Secondary structure assignment per residue plotted against time. (d) Root-mean-square fluctuations (RMSF) of  $C_{\alpha}$  atoms of individual residues from each monomer of C–C<sup>AP</sup> dimer.

On the other hand, the most representative structure derived in the second case ( $X^P-O^2$ ) retains all the key structural features of  $X^P$  (Figure S9, Supporting Information). The intermolecular  $\beta$ -sheet (Lys28-Ala33 (M1)–Ala30-Gly37 (M2)), content of the secondary structures, and the Glu22(M1)-Lys28(M2) salt-bridge are retained in this structure. The starting structure (the most representative structure derived from the  $X^P$  simulation) used here was so stable that a change in the force field from GROMOS to OPLS did not influence its structural properties.

**IIIa1. Translational and Rotational Dynamics of the  $X^P$  Dimer.** The translational diffusion constant ( $D_T$ ) and rotational diffusion constant ( $D_R$ ) are associated with the size and shape of the dimer. The  $D_T$  and  $D_R$  values of  $A\beta40$  and  $A\beta42$  monomers computed in our previous study<sup>111</sup> were in excellent agreement with the experimentally measured values.<sup>69,70</sup> Here, exactly the same approach has been employed to compute these parameters for the  $X^P$  dimer.

$D_T$  is computed by fitting the linear region (first 5 ns region of the production phase of 50 ns simulation) to the Einstein–Stokes relation  $D_T = \lim_{t \rightarrow \infty} (1/6t) \langle |r(t) - r(0)|^2 \rangle$  (eq 1, Supporting Information). The time dependent variation of mean square displacement (MSD) of this dimer is shown in

Figure 3a. Since the SPC water model overestimates the diffusion constant of water by a factor of 1.80 at 300 K,<sup>112</sup> the correction that accounts for this overestimation has been made in the reported value. The corrected  $D_T$  value of  $0.63 \times 10^{-6}$  cm<sup>2</sup>/s is  $0.8 \times 10^{-6}$  cm<sup>2</sup>/s lower than the one computed for the monomer ( $1.43 \times 10^{-6}$  cm<sup>2</sup>/s).<sup>111</sup> This value is qualitatively in agreement with the fact that the increase of hydrodynamic radius or molecular weight must result in the decrease of the self-diffusion constant of the molecule. The experimentally measured value for the  $A\beta42$  dimer is not currently available.

Since the global and internal motions exert a combined influence on the time dependent dynamics of the peptide,  $D_R$  cannot be derived directly from the MD generated trajectories. The first step in its calculation involves the decoupling of the global tumbling and internal motions to utilize the former for the computation of  $D_R$ . Prior to the separation of global and internal motions from the MD generated trajectory, it was confirmed that they occur in two different time scales. The total average and individual correlation functions ( $C_{\text{tot}}^{\text{ave}}(t)$  and  $C_{\text{tot}}(t)$ ) averaged over all the N–H backbone bond vectors of Ala2–Ala42 amino acid residues of both M1 and M2 were obtained directly from the 50 ns production phase of the MD

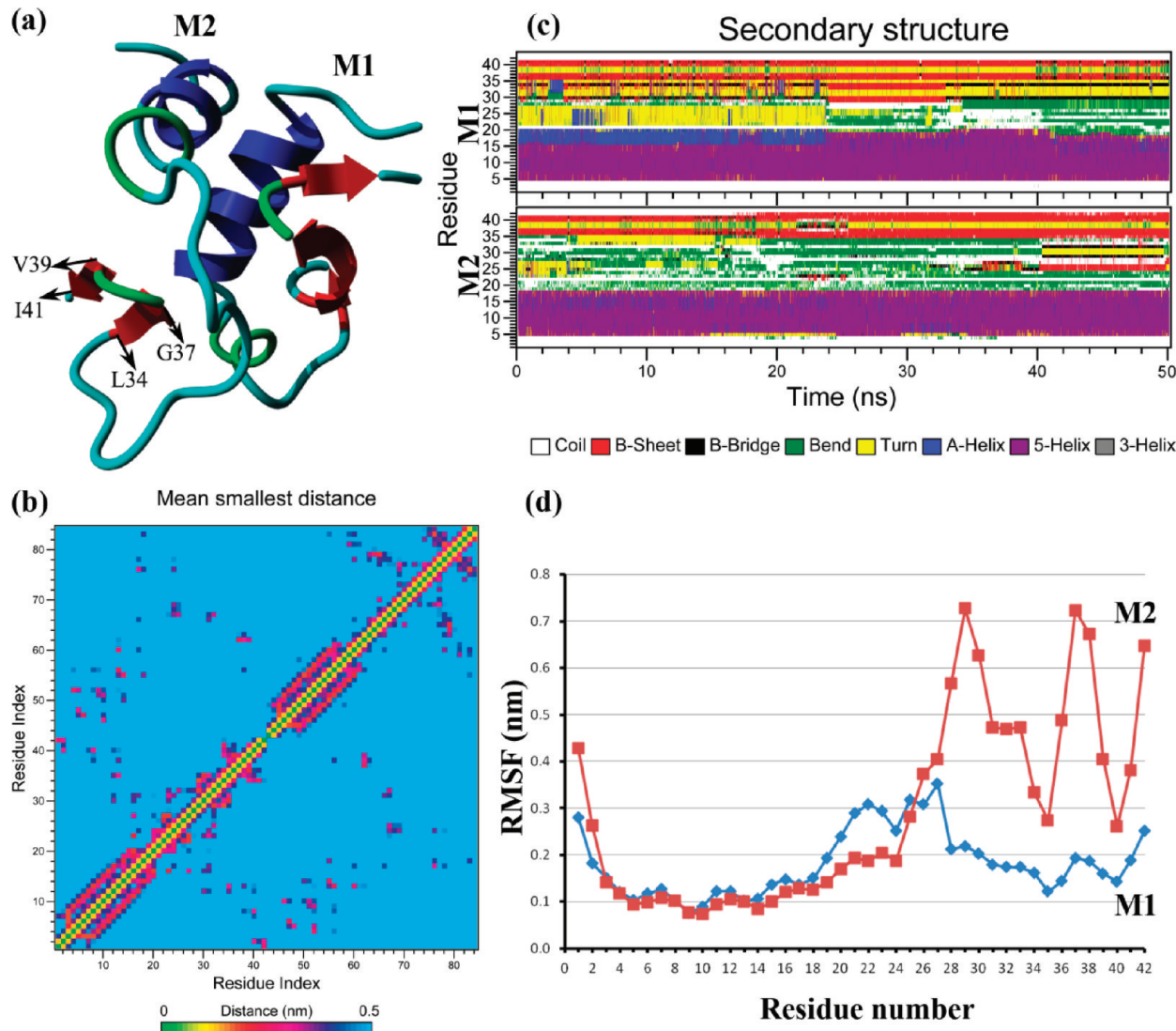


**Figure 5.** (a) Cartoon presentation of the most representative structure obtained by cluster analysis performed on 50 ns simulation in the production phase. (b) Contact map, where each square provides the mean average distance (intensity coded) of heavy atoms for the side chains of the residues which are less than 0.5 nm apart. (c) Secondary structure assignment per residue plotted against time. (d) Root-mean-square fluctuations (RMSF) of  $C_{\alpha}$  atoms of individual residues from each monomer of  $N-N'$  dimer.

simulation. The first 10 ns of  $C_{\text{tot}}^{\text{ave}}(t)$  functions derived from the entire production phase trajectory (black line) and four fitting models to the product correlation functions (Figure 3b). The equations used to model the rotational motion (eq 2), and the internal motion (Lipari-Szabo (eq 3), Clore-Szabo (eq 4), and modified Clore-Szabo (eq 5)) are provided in the Supporting Information. The fitting of  $C_{\text{tot}}^{\text{ave}}(t)$  to eq 2 indicates that the total correlation function is not mono-exponential (the red line in Figure 3b). For the internal correlation function, the fitting using eq 2 coupled with the Lipari-Szabo (eq 3), the Clore-Szabo (eq 4), and modified Clore-Szabo (eq 5) models are shown in green, purple, and blue lines, respectively (Figure 3b). All these three fitted correlation curves could reproduce the long time scales. However, the short-term behavior of  $C_{\text{tot}}^{\text{ave}}(t)$  and the fitted model functions indicate that only the Clore-Szabo model (eq 4) best fitted to  $C_{\text{tot}}^{\text{ave}}(t)$  at the short as well as long time scales (purple line in the inset of Figure 3b). This clearly indicates that the total correlation function includes contributions from both rotational ( $C_{\text{rot}}(t)$ ) and internal ( $C_{\text{int}}(t)$ ) motions that occur in nano- and picosecond time

scales, respectively. The separation of the rotational and internal motions in this step allows the extraction of rotational trajectory (free from internal motions) through the procedure outlined in our previous study.<sup>111</sup>

This trajectory is now used to derive the average  $C_{\text{rot}}^{\text{ave}}(t)$  and individual rotational correlation functions  $C_{\text{rot}}(t)$  for each backbone N–H bond vector of the Ala2–Ala42 residues of the  $X^P$  dimer (Figure 3c).  $C_{\text{rot}}(t)$  of each vector was fitted to the mono-exponential decay function (eq 2) to obtain the rotational correlation time  $\tau_{\text{rot}}$  of each backbone N–H bond vector. This fitting is in good agreement for randomly chosen Lys28 and Ile32 residues (Figure 3d and e) and the remaining N–H dipole vectors (black and red lines in Figure 3d and e represent  $C_{\text{rot}}(t)$  obtained from the MD simulation and the mono-exponential fit of  $C_{\text{rot}}(t)$  using eq 2, respectively). From  $\tau_{\text{rot}}$ , the computed  $D_R$  value using eq 6 in the Supporting Information is  $0.063 \text{ ns}^{-1}$ . The inclusion of a correction for the SPC water model provides a value of  $0.035 \text{ ns}^{-1}$ . This value of  $D_R$  is 50% smaller than  $0.071 \text{ ns}^{-1}$  computed for the  $A\beta42$

monomer,<sup>111</sup> which indicates that an increase in the molecular weight of  $\text{A}\beta 42$  by 2 times reduces its  $D_R$  by half.

**IIIb. Structural Features of the C–C<sup>AP</sup> Dimer.** The antiparallel alignment of the C-termini (Asp27-Ala42) of M1 and M2 leads to the formation of the C–C<sup>AP</sup> dimer (Figure 1). The C-terminus of  $\text{A}\beta 42$  includes SHR (Gly29-Met35) and Ile41-Ala42 dipeptide that are previously proposed to be critical for aggregation.<sup>58</sup> The Ile41 residue of the dipeptide has been reported to be involved in the formation of paranuclei for fibrillation.<sup>48</sup> Furthermore, the  $\text{A}\beta(29\text{--}40)$  fragment has been observed to form amyloid fibrils by itself.<sup>107</sup> Therefore, the detailed conformational changes in the 29–42 region of the full-length  $\text{A}\beta 42$  during the dimerization will provide better understanding of its role in the aggregation.

The dimerization from this configuration proceeds through the formation of multiple hydrophobic and hydrogen bonding interactions between the SHR and C-terminus regions of both monomers (M1 and M2). In the most representative structure of this dimer, the Leu34-Val36 region of M1 and Val39-Ile41 region of M2, respectively, form the antiparallel intra  $\beta$ -sheet structures connected by a turn region (Figure 4a). The Leu34-Gly37 regions of both monomers also interact with each other through parallel  $\beta$ -sheets. These structural features are consistent with a model of  $\text{A}\beta 42$  oligomer suggested in a NMR study.<sup>113</sup> The contact maps of this dimer show strong hydrogen bonds ( $\sim 1.9 \text{ \AA}$ ) between His13, Gly33, Met35, and Gly37 of M1 and Gly37, Lys28, Met35, and Gly37 of M2, respectively (Figure 4b). In addition, the Leu34 and Met35 residues of M1 form hydrophobic interactions with Ile31 and Leu34 of M2, respectively.

The rmsd's of the CHC, TR, and SHR regions of both M1 and M2 showed that they undergo substantial conformational changes during the simulation (Figure S3b, Supporting Information). The Val24-Asn27 region of M1 randomly alters between turn and bend conformations (Figure 4c). In M2, this region is mostly dominated by the turn structure. The presence of dominant turn conformation in this region is also in line with the recent NMR studies on  $\text{A}\beta$  oligomerization.<sup>113</sup> It was reported that the relative kinetic and thermodynamic stability of the bend (leads to fibrils) or the turn (leads to globulomers) is critical for aggregation. The SHR segment of M1 and M2 stays in stable bend and random coil structures throughout the simulation (Figure 4c). However, in comparison to M1, the percentage of random coil structure is higher in M2.

The atomic positional fluctuations of the  $C_\alpha$  atoms indicate that the residues in the N-terminal and TR regions of both monomers are more mobile than the ones in CHC, SHR, and C-terminal segments (Figure 4d). The observed rigidity of the CHC region is caused by the intermolecular interactions between M1 and M2, whereas in SHR and C-terminus it is due to both inter- and intramolecular interactions between the monomers. Similar to the salt-bridge between Glu22(M1) and Lys28(M2) in X<sup>P</sup>, a salt-bridge between Asp23(M2) and Lys28(M1) is formed in this dimer. The existence of this salt-bridge is also supported by the ssNMR data on  $\text{A}\beta$  fibrils and MD simulations on the  $\text{A}\beta(1\text{--}39)$  dimer.<sup>37,51,52,54,66</sup> The time dependent variation of the distance between Asp23(M2) and Lys28(M1) shows that this salt-bridge is formed after the first 17 ns of the simulation (Figure S5b, Supporting Information).

**IIIc. Structural Features of the N–N<sup>P</sup> Dimer.** The N–N<sup>P</sup> dimer is formed by positioning the parallel N-termini and the CHC regions of M1 and M2 parallel to each other in the starting configuration (Figure 1). The N-terminus consists of

the CHC (Leu17-Ala21) region, which has been experimentally reported to be involved in the aggregation process.<sup>55</sup> The Val12-Val24 fragment was also observed to form the  $\beta$ -sheet structure in the fully formed fibrils.<sup>51</sup> Furthermore, Balbach and co-workers reported that  $\text{A}\beta(16\text{--}22)$  is the shortest fragment to form amyloid fibrils.<sup>114</sup> The detailed conformational changes occurring in the CHC region will help with understanding of its role in the dimerization.

The generation of the N–N<sup>P</sup> dimer occurs via the formation of several intermolecular interactions such as hydrophobic interactions,  $\pi$ – $\pi$  stacking, and hydrogen bonding between the N-termini of both monomers. The most representative structure derived from the N–N<sup>P</sup> simulations is shown in Figure 5a. During the simulation, M1 retains its initial hairpin-like structure and only M2 undergoes drastic conformational changes. In the N–N<sup>P</sup> dimer, the His6-Val18 and Ala30-Gly33 segments of M1 and His6-Glu11 of M2 exist in the  $\alpha$ -helical conformations and the Leu34-Gly37 and Val39-Ile41 region of M1 and Leu34-Gly37 and Val39-Ala42 of M2 form antiparallel  $\beta$ -sheet structures, respectively. The contact map of this dimer (Figure 5b) shows interactions between Phe4, Arg5, His6, Tyr10, His13, Leu17, and Val18 of M1 with Tyr10, Phe4, Val18, Leu17, and Leu34 of M2, respectively. In particular, His6 (M1) forms a hydrogen bond with Arg5 (M2) and the side chains of Phe4, Arg5, Tyr10, His13, and Leu17 of M1 interact through hydrophobic interactions with Tyr10, Tyr10, Phe4, Val18, and Leu34 of M2, respectively.

The CHC region of M1 exists as a stable  $\alpha$ -helix for the first 24 ns, but after that, it stays as an open 5-helix for the rest of the simulation (Figure 5c). On the other hand, the Leu17-Val18 and Phe19-Ala21 segments of M2 stay in stable 5-helix and bend structures throughout the simulation. The TR (Val24-Asn27) in M1 retains the turn conformation for the first 24 ns, but after that, it converts into a bend structure with the occasional appearance of a random coil. However, TR in M2 undergoes substantial structural changes and alters between turn, bend, and random coil conformations. There were no noticeable changes in the SHR and C-terminus of M1, and they exist in the stable  $\beta$ -sheet–turn– $\beta$ -sheet conformation during the simulation. However, only the SHR region of M2 is quite flexible and changes from bend → turn → bend → coil structures. The maximum atomic positional fluctuations of the  $C_\alpha$  atoms in M1 and M2 are observed in the TR and C-terminus, respectively (Figure 5d). The rigidity in the C-terminal region of M1 is due to the formation of several intramolecular interactions with the N-terminus. In both monomers, the minimum fluctuations are observed in the (Phe4-Glu22) region. It is worth mentioning that unlike X<sup>P</sup> and C–C<sup>AP</sup> no salt-bridge between Glu22/Asp23-Lys28 formed in this dimer.

These results indicate that hydrophobic interactions between the CHC regions of both monomers drive the formation of this dimer. The formation of this dimer is also supported by NMR data, which suggests that this region is critical for aggregation.<sup>55</sup>

#### IV. SUMMARY AND CONCLUSIONS

In conclusion, in the present study, MD simulations have been employed to elucidate the mechanism of the  $\text{A}\beta 42$  dimerization and the roles of specific regions (N-terminus, CHC, TR, SHR, and C-terminus) in this process. On the basis of the interactions between different regions, 10 different starting configurations were developed from the native folded structures of monomers. Out of these configurations, only six (N–N<sup>P</sup>, X<sup>P</sup>,

$X^{AP}$ ,  $C-C^{AP}$ ,  $N-N^{AP}$ , and  $N-C^{AP}$ ) were found to form dimeric structures. On the basis of the computed electrostatic binding energies, the structural characteristics of the three most stable dimers ( $X^P$ ,  $C-C^{AP}$ , and  $N-N^P$ ) are discussed.

The simulations show that the hydrophobic regions comprising CHC and SHR play crucial roles in the formation and stabilization of  $A\beta$ 42 dimers. The high content of  $\alpha$ -helix observed in all six dimers is in accordance with the experimental observation that the  $\alpha$ -helical conformation is a key intermediate in  $A\beta$  aggregation.<sup>102,115,116</sup> The  $X^P$  dimer is formed by the formation of a zipper between the Lys28-Ala33 and Ala30-Gly37 regions of M1 and M2, respectively. The formation of the zipper has also been experimentally proposed in aggregation of several amyloidogenic peptides including  $A\beta$ .<sup>38,106</sup> The translational diffusion constant ( $D_T$ ) and rotational diffusion constant ( $D_R$ ) of  $X^P$  are calculated to be  $0.63 \times 10^{-6} \text{ cm}^2/\text{s}$  and  $0.035 \text{ ns}^{-1}$ , respectively. These constants can be utilized to estimate the interaction parameters of these peptides through the measurement of diffusion coefficients at different peptide concentrations. They can also help to characterize the aggregation state of oligomers in solution. The formation of the salt-bridge between Glu22/Asp23 and Lys28 of different monomers in the  $X^P$  and  $C-C^{AP}$  dimers is consistent with the recent NMR and theoretical predictions.<sup>37,51,52,54,60–66</sup> In the  $C-C^{AP}$  dimer, the formation of antiparallel (between Leu34-Val36 (M1) and Val39-Ile41 (M2)) and parallel (between Leu34-Gly37 (M1) and Leu34-Gly37 (M1))  $\beta$ -sheets is in line with NMR data on  $A\beta$ 42 oligomers.<sup>113</sup> The generation of the  $N-N^P$  dimer through the hydrophobic interactions between the CHC regions of both monomers is also supported by NMR data.<sup>55</sup>

The results presented in this study have provided detailed information regarding the dimerization mechanism of the critical  $A\beta$ 42 peptide and structural properties of different conformers. This information may pave the way to develop therapeutic strategies for the prevention and treatment of AD.

## ASSOCIATED CONTENT

### Supporting Information

(a) Equations 1–6; (b) Figures S1–S9; (c) full citations including all authors for refs 11, 18, 24, 25, 32, 104, 106, and 113. This material is available free of charge via the Internet at <http://pubs.acs.org>.

## AUTHOR INFORMATION

### Corresponding Author

\*E-mail: rpr@miami.edu. Phone: 305-284-9372. Fax: 305-284-4571.

### Notes

The authors declare no competing financial interest.

## ACKNOWLEDGMENTS

A funding grant (DOH grant number 08KN-11) to R.P. from the James and Esther King Biomedical Research Program of the Florida State Health Department is acknowledged. Computational resources from the Center for Computational Science (CCS) at the University of Miami are greatly appreciated. We thank Erica Sturm for her assistance in the preparation of the manuscript.

## REFERENCES

- (1) Mattson, M. P. *Nature* 2004, 430, 631–639.
- (2) Hardy, J.; Selkoe, D. J. *Science* 2002, 297, 353–356.
- (3) Klein, W. L.; Krafft, G. A.; Finch, C. E. *Trends Neurosci.* 2001, 24, 219–224.
- (4) Selkoe, D. J. *Nat. Cell Biol.* 2004, 6, 1054–1061.
- (5) Kirkitadze, M. D.; Bitan, G.; Teplow, D. B. *J. Neurosci. Res.* 2002, 69, 567–577.
- (6) Klein, W. L. *Neurobiol. Aging* 2002, 23, 231–233.
- (7) Hardy, J. *Ann. Neurol.* 2003, 54, 143–144.
- (8) Klein, W. L.; Stine, W. B., Jr.; Teplow, D. B. *Neurobiol. Aging* 2004, 25, 569–580.
- (9) Seubert, P.; Vigo-Pelfrey, C.; Esch, F.; Lee, M.; Dovey, H.; Davis, D.; Sinha, S.; Schlossmacher, M.; Whaley, J.; Swindlehurst, C. *Nature* 1992, 359, 325–327.
- (10) Haass, C.; Schlossmacher, M.; Hung, A.; Vigo-Pelfrey, C.; Mellon, A.; Ostaszewski, B.; Lieberburg, I.; Koo, E.; Schenk, D.; Teplow, D. *Nature* 1992, 359, 322–325.
- (11) Shoji, M.; Golde, T.; Ghiso, J.; Cheung, T.; Estus, S.; Shaffer, L.; Cai, X.; McKay, D.; Tintner, R.; Frangione, B.; et al. *Science* 1992, 258, 126–129.
- (12) Dahlgren, K. N.; Manelli, A. M.; Stine, W. B.; Baker, L. K.; Krafft, G. A.; LaDu, M. J. *J. Biol. Chem.* 2002, 277, 32046–32053.
- (13) Pillot, T.; Drouet, B.; Queillé, S.; Labeyre, C.; Vandekerckhove, J.; Rosseneu, M.; Pinçon-Raymond, M.; Chambaz, J. *J. Neurochem.* 1999, 73, 1626–1634.
- (14) Suo, Z.; Humphrey, J.; Kundtz, A.; Sethi, F.; Placzek, A.; Crawford, F.; Mullan, M. *Neurosci. Lett.* 1998, 257, 77–80.
- (15) Younkin, S. G. *Ann. Neurol.* 1995, 37, 287–288.
- (16) Corder, E.; Saunders, A.; Strittmatter, W.; Schmeichel, D.; Gaskell, P.; Small, G.; Roses, A.; Haines, J.; Pericak-Vance, M. *Science* 1993, 261, 921–923.
- (17) Walsh, D. M.; Lomakin, A.; Benedek, G. B.; Condron, M. M.; Teplow, D. B. *J. Biol. Chem.* 1997, 272, 22364–22372.
- (18) Rovelet-Leroux, A.; Hannequin, D.; Raux, G.; Meur, N. L.; Laquerrière, A.; Vital, A.; Dumanchin, C.; Feuillette, S.; Brice, A.; Vercelletto, M.; et al. *Nat. Genet.* 2006, 38, 24–26.
- (19) Pike, C. J.; Walencewicz, A. J.; Glabe, C. G.; Cotman, C. W. *Brain Res.* 1991, 563, 311–314.
- (20) Levy, E.; Carman, M.; Fernandez-Madrid, I.; Power, M.; Lieberburg, I.; van Duinen, S.; Bots, G.; Luyendijk, W.; Frangione, B. *Science* 1990, 248, 1124–1126.
- (21) Bentahir, M.; Nyabi, O.; Verhamme, J.; Tolia, A.; Horré, K.; Wiltfang, J.; Esselmann, H.; De Strooper, B. *J. Neurochem.* 2006, 96, 732–742.
- (22) Hsia, A. Y.; Masliah, E.; McConlogue, L.; Yu, G.-Q.; Tatsuno, G.; Hu, K.; Khodenko, D.; Malenka, R. C.; Nicoll, R. A.; Mucke, L. *Proc. Natl. Acad. Sci. U.S.A.* 1999, 96, 3228–3233.
- (23) Deshpande, A.; Mina, E.; Glabe, C.; Busciglio, J. *J. Neurosci.* 2006, 26, 6011–6018.
- (24) Roher, A. E.; Chaney, M. O.; Kuo, Y.-M.; Webster, S. D.; Stine, W. B.; Haverkamp, L. J.; Woods, A. S.; Cotter, R. J.; Tuohy, J. M.; Krafft, G. A.; et al. *J. Biol. Chem.* 1996, 271, 20631–20635.
- (25) Shankar, G. M.; Li, S.; Mehta, T. H.; Garcia-Munoz, A.; Shepardson, N. E.; Smith, I.; Brett, F. M.; Farrell, M. A.; Rowan, M. J.; Lemere, C. A.; et al. *Nat. Med.* 2008, 14, 837–842.
- (26) Walsh, D. M.; Klyubin, I.; Fadeeva, J. V.; Cullen, W. K.; Anwyl, R.; Wolfe, M. S.; Rowan, M. J.; Selkoe, D. J. *Nature* 2002, 416, 535–539.
- (27) Soreghan, B.; Kosmoski, J.; Glabe, C. *J. Biol. Chem.* 1994, 269, 28551–28554.
- (28) Garzon-Rodriguez, W.; Sepulveda-Becerra, M.; Milton, S.; Glabe, C. G. *J. Biol. Chem.* 1997, 272, 21037–21044.
- (29) Garzon-Rodriguez, W.; Vega, A.; Sepulveda-Becerra, M.; Milton, S.; Johnson, D. A.; Yatsimirska, A. K.; Glabe, C. G. *J. Biol. Chem.* 2000, 275, 22645–22649.
- (30) Riek, R.; Güntert, P.; Döbeli, H.; Wipf, B.; Wüthrich, K. *Eur. J. Biochem.* 2001, 268, 5930–5936.
- (31) Zhang, S.; Iwata, K.; Lachenmann, M. J.; Peng, J. W.; Li, S.; Stimson, E. R.; Lu, Y. a.; Felix, A. M.; Maggio, J. E.; Lee, J. P. *J. Struct. Biol.* 2000, 130, 130–141.

- (32) Hou, L.; Shao, H.; Zhang, Y.; Li, H.; Menon, N. K.; Neuhaus, E. B.; Brewer, J. M.; Byeon, I.-J. L.; Ray, D. G.; Vitek, M. P.; et al. *J. Am. Chem. Soc.* **2004**, *126*, 1992–2005.
- (33) Wei, G.; Shea, J.-E. *Biophys. J.* **2006**, *91*, 1638–1647.
- (34) Massi, F.; Peng, J. W.; Lee, J. P.; Straub, J. E. *Biophys. J.* **2001**, *80*, 31–44.
- (35) Baumketner, A.; Shea, J.-E. *J. Mol. Biol.* **2006**, *362*, 567–579.
- (36) Baumketner, A.; Shea, J.-E. *J. Mol. Biol.* **2007**, *366*, 275–285.
- (37) Anand, P.; Nandel, F. S.; Hansmann, U. H. *E. J. Chem. Phys.* **2008**, *129*, 195102–195107.
- (38) Hwang, W.; Zhang, S.; Kamm, R. D.; Karplus, M. *Proc. Natl. Acad. Sci. U.S.A.* **2004**, *101*, 12916–12921.
- (39) Itoh, S. G.; Okamoto, Y. *J. Phys. Chem. B* **2008**, *112*, 2767–2770.
- (40) Tarus, B.; Straub, J. E.; Thirumalai, D. *J. Mol. Biol.* **2005**, *345*, 1141–1156.
- (41) Gnanakaran, S.; Nussinov, R.; García, A. E. *J. Am. Chem. Soc.* **2006**, *128*, 2158–2159.
- (42) Huet, A.; Derreumaux, P. *Biophys. J.* **2006**, *91*, 3829–3840.
- (43) Lu, Y.; Wei, G.; Derreumaux, P. *J. Phys. Chem. B* **2011**, *115*, 1282–1288.
- (44) Nguyen, P. H.; Li, M. S.; Derreumaux, P. *Phys. Chem. Chem. Phys.* **2011**, *13*, 9778–9788.
- (45) Luttmann, E.; Fels, G. *Chem. Phys.* **2006**, *323*, 138–147.
- (46) Xu, Y.; Shen, J.; Luo, X.; Zhu, W.; Chen, K.; Ma, J.; Jiang, H. *Proc. Natl. Acad. Sci. U.S.A.* **2005**, *102*, 5403–5407.
- (47) Urbanc, B.; Cruz, L.; Ding, F.; Sammond, D.; Khare, S.; Buldyrev, S. V.; Stanley, H. E.; Dokholyan, N. V. *Biophys. J.* **2004**, *87*, 2310–2321.
- (48) Bitan, G.; Kirkpatridge, M. D.; Lomakin, A.; Vollmers, S. S.; Benedek, G. B.; Teplow, D. B. *Proc. Natl. Acad. Sci. U.S.A.* **2003**, *100*, 330–335.
- (49) Bitan, G.; Lomakin, A.; Teplow, D. B. *J. Biol. Chem.* **2001**, *276*, 35176–35184.
- (50) Bitan, G.; Teplow, D. B. *Acc. Chem. Res.* **2004**, *37*, 357–364.
- (51) Petkova, A. T.; Ishii, Y.; Balbach, J. J.; Antzutkin, O. N.; Leapman, R. D.; Delaglio, F.; Tycko, R. *Proc. Natl. Acad. Sci. U.S.A.* **2002**, *99*, 16742–16747.
- (52) Petkova, A. T.; Yau, W.-M.; Tycko, R. *Biochemistry* **2006**, *45*, 498–512.
- (53) Paravastu, A. K.; Petkova, A. T.; Tycko, R. *Biophys. J.* **2006**, *90*, 4618–4629.
- (54) Petkova, A. T.; Leapman, R. D.; Guo, Z. H.; Yau, W. M.; Mattson, M. P.; Tycko, R. *Science* **2005**, *307*, 262–265.
- (55) Tjernberg, L. O.; Näslund, J.; Lindqvist, F.; Johansson, J.; Karlström, A. R.; Thyberg, J.; Terenius, L.; Nordstedt, C. *J. Biol. Chem.* **1996**, *271*, 8545–8548.
- (56) Shivaprasad, S.; Wetzel, R. *Biochemistry* **2004**, *43*, 15310–15317.
- (57) Török, M.; Milton, S.; Kayed, R.; Wu, P.; McIntire, T.; Glabe, C. G.; Langen, R. *J. Biol. Chem.* **2002**, *277*, 40810–40815.
- (58) Pike, C. J.; Walencewicz-Wasserman, A. J.; Kosmoski, J.; Cribbs, D. H.; Glabe, C. G.; Cotman, C. W. *J. Neurochem.* **1995**, *64*, 253–265.
- (59) Esler, W. P.; Stimson, E. R.; Ghilardi, J. R.; Lu, Y.-A.; Felix, A. M.; Vinters, H. V.; Mantyh, P. W.; Lee, J. P.; Maggio, J. E. *Biochemistry* **1996**, *35*, 13914–13921.
- (60) Ma, B.; Nussinov, R. *Proc. Natl. Acad. Sci. U.S.A.* **2002**, *99*, 14126–14131.
- (61) Massi, F.; Klimov, D.; Thirumalai, D.; Straub, J. E. *Protein Sci.* **2002**, *11*, 1639–1647.
- (62) Thirumalai, D.; Klimov, D. K.; Dima, R. I. *Curr. Opin. Struct. Biol.* **2003**, *13*, 146–159.
- (63) Dima, R. I.; Thirumalai, D. *Bioinformatics* **2004**, *20*, 2345–2354.
- (64) Lührs, T.; Ritter, C.; Adrian, M.; Riek-Lohr, D.; Bohrmann, B.; Döbeli, H.; Schubert, D.; Riek, R. *Proc. Natl. Acad. Sci. U.S.A.* **2005**, *102*, 17342–17347.
- (65) Sciarretta, K. L.; Gordon, D. J.; Petkova, A. T.; Tycko, R.; Meredith, S. C. *Biochemistry* **2005**, *44*, 6003–6014.
- (66) Buchete, N.-V.; Hummer, G. *Biophys. J.* **2007**, *92*, 3032–3039.
- (67) Altieri, A. S.; Hinton, D. P.; Byrd, R. A. *J. Am. Chem. Soc.* **1995**, *117*, 7566–7567.
- (68) Baldwin, A. J.; Anthony-Cahill, S. J.; Knowles, T. P. J.; Lippens, G.; Christodoulou, J.; Barker, P. D.; Dobson, C. M. *Angew. Chem., Int. Ed.* **2008**, *47*, 3385–3387.
- (69) Danielsson, J.; Jarvet, J.; Damberg, P.; Gräslund, A. *Magn. Reson. Chem.* **2002**, *40*, S89–S97.
- (70) Danielsson, J.; Andersson, A.; Jarvet, J.; Gräslund, A. *Magn. Reson. Chem.* **2006**, *44*, S114–S121.
- (71) Berendsen, H. J. C.; van der Spoel, D.; van Drunen, D. *Comput. Phys. Commun.* **1995**, *91*, 43–56.
- (72) Lindahl, E.; Hess, B.; van der Spoel, D. *J. Mol. Model.* **2001**, *7*, 306–317.
- (73) Oostenbrink, C.; Villa, A.; Mark, A. E.; van Gunsteren, W. F. *J. Comput. Chem.* **2004**, *25*, 1656–1676.
- (74) Zagrovic, B.; Gattin, Z.; Lau, J.; Huber, M.; van Gunsteren, W. *Eur. Biophys. J.* **2008**, *37*, 903–912.
- (75) Schwab, F.; Gunsteren, W. F. v.; Zagrovic, B. *Biochemistry* **2008**, *47*, 2945–2951.
- (76) Vögeli, B.; Segawa, T. F.; Leitz, D.; Sobol, A.; Choutko, A.; Trzesniak, D.; van Gunsteren, W.; Riek, R. *J. Am. Chem. Soc.* **2009**, *131*, 17215–17225.
- (77) Mai, B. K.; Viet, M. H.; Li, M. S. *J. Chem. Inf. Model.* **2010**, *50*, 2236–2247.
- (78) Berendsen, H. J. C.; Postma, J. P. M.; van Gunsteren, W. F.; Hermans, J. *Interaction Models for Water in Relation to Protein Hydration*; D. Reider Publishing Company: Dordrecht, The Netherlands, 1981.
- (79) Miyamoto, S.; Kollman, P. A. *J. Comput. Chem.* **1992**, *13*, 952–062.
- (80) Hess, B.; Bekker, H.; Berendsen, H. J. C.; Fraaije, J. G. E. M. *J. Comput. Chem.* **1997**, *18*, 1463–1472.
- (81) Darden, T. A.; York, D.; Pedersen, L. *J. Chem. Phys.* **1993**, *98*, 10089–10092.
- (82) York, D. M.; Wlodawer, A.; Pedersen, L. G.; Darden, T. A. *Proc. Natl. Acad. Sci. U.S.A.* **1994**, *91*, 8715–8718.
- (83) Krieger, E.; Vriend, G. *Bioinformatics* **2002**, *18*, 315–318.
- (84) Kabsch, W.; Sander, C. *Biopolymers* **1983**, *22*, 2577–2637.
- (85) Daura, X.; van Gunsteren, W. F.; Mark, A. E. *Proteins: Struct., Funct., Genet.* **1999**, *34*, 269–280.
- (86) Triguero, L.; Singh, R.; Prabhakar, R. *J. Phys. Chem. B* **2008**, *112*, 7123–7131.
- (87) Crescenzi, O.; Tomaselli, S.; Guerrini, R.; Salvadori, S.; D'Ursi, A. M.; Temussi, P. A.; Picone, D. *Eur. J. Biochem.* **2002**, *269*, 5642–5648.
- (88) Triguero, L.; Singh, R.; Prabhakar, R. *J. Phys. Chem. B* **2008**, *112*, 2159–2167.
- (89) Shen, L.; Ji, H.-F.; Zhang, H.-Y. *J. Phys. Chem. B* **2008**, *112*, 3164–3167.
- (90) Nordling, E.; Kallberg, Y.; Johansson, J.; Persson, B. *J. Comput.-Aided Mol. Des.* **2008**, *22*, 53–58.
- (91) Tomaselli, S.; Esposito, V.; Vangone, P.; van Nuland, N. A. J.; Bonvin, A. M. J. J.; Guerrini, R.; Tancredi, T.; Temussi, P. A.; Picone, D. *ChemBioChem* **2006**, *7*, 257–267.
- (92) Jorgensen, W. L.; Tirado-Rives, J. *J. Am. Chem. Soc.* **1988**, *110*, 1657–1666.
- (93) Kaminski, G. A.; Friesner, R. A.; Tirado-Rives, J.; Jorgensen, W. L. *J. Phys. Chem. B* **2001**, *105*, 6474–6487.
- (94) Tirado-Rives, J.; Jorgensen, W. L. *Biochemistry* **1991**, *30*, 3864–3871.
- (95) Baker, N.; Holst, M.; Wang, F. *J. Comput. Chem.* **2000**, *21*, 1343–1352.
- (96) Baker, N. A.; Sept, D.; Joseph, S.; Holst, M. J.; McCammon, J. A. *Proc. Natl. Acad. Sci. U.S.A.* **2001**, *98*, 10037–10041.
- (97) Pérez, C.; Pastor, M.; Ortiz, A. R.; Gago, F. *J. Med. Chem.* **1998**, *41*, 836–852.
- (98) Dolinsky, T. J.; Nielsen, J. E.; McCammon, J. A.; Baker, N. A. *Nucleic Acids Res.* **2004**, *32*, W665–W667.

- (99) Dolinsky, T. J.; Czodrowski, P.; Li, H.; Nielsen, J. E.; Jensen, J. H.; Klebe, G.; Baker, N. A. *Nucleic Acids Res.* **2007**, *35*, W522–W525.
- (100) Sharp, K.; Nicholls, A.; Fine, R.; Honig, B. *Science* **1991**, *252*, 106–109.
- (101) Sitkoff, D.; Sharp, K. A.; Honig, B. *J. Phys. Chem.* **1994**, *98*, 1978–1988.
- (102) Kirkitadze, M. D.; Condron, M. M.; Teplow, D. B. *J. Mol. Biol.* **2001**, *312*, 1103–1119.
- (103) Hung, L. W.; Ciccotto, G. D.; Giannakis, E.; Tew, D. J.; Perez, K.; Masters, C. L.; Cappai, R.; Wade, J. D.; Barnham, K. J. *J. Neurosci.* **2008**, *28*, 11950–11958.
- (104) Harmeier, A.; Wozny, C.; Rost, B. R.; Munter, L.-M.; Hua, H.; Georgiev, O.; Beyermann, M.; Hildebrand, P. W.; Weise, C.; Schaffner, W.; et al. *J. Neurosci.* **2009**, *29*, 7582–7590.
- (105) Munter, L.-M.; Voigt, P.; Harmeier, A.; Kaden, D.; Gottschalk, K. E.; Weise, C.; Pipkorn, R.; Schaefer, M.; Langosch, D.; Multhaup, G. *EMBO J.* **2007**, *26*, 1702–1712.
- (106) Sawaya, M. R.; Sambashivan, S.; Nelson, R.; Ivanova, M. I.; Sievers, S. A.; Apostol, M. I.; Thompson, M. J.; Balbirnie, M.; Wiltzius, J. J. W.; McFarlane, H. T.; et al. *Nature* **2007**, *447*, 453–457.
- (107) Barrow, C. J.; Yasuda, A.; Kenny, P. T. M.; Zagorski, M. G. *J. Mol. Biol.* **1992**, *225*, 1075–1093.
- (108) Hilbich, C.; Kisters-Woike, B.; Reed, J.; Masters, C. L.; Beyreuther, K. *J. Mol. Biol.* **1991**, *218*, 149–163.
- (109) Sgourakis, N. G.; Yan, Y.; McCallum, S. A.; Wang, C.; Garcia, A. E. *J. Mol. Biol.* **2007**, *368*, 1448–1457.
- (110) Sgourakis, N. G.; Merced-Serrano, M.; Boutsidis, C.; Drineas, P.; Du, Z.; Wang, C.; Garcia, A. E. *J. Mol. Biol.* **2011**, *405*, 570–583.
- (111) Bora, R. P.; Prabhakar, R. *J. Chem. Phys.* **2009**, *131*, 1551031–15510311.
- (112) Smith, P. E.; van Gunsteren, W. F. *Chem. Phys. Lett.* **1993**, *215*, 315–318.
- (113) Yu, L.; Edalji, R.; Harlan, J. E.; Holzman, T. F.; Lopez, A. P.; Labkovsky, B.; Hillen, H.; Barghorn, S.; Ebert, U.; Richardson, P. L.; et al. *Biochemistry* **2009**, *48*, 1870–1877.
- (114) Balbach, J. J.; Ishii, Y.; Antzutkin, O. N.; Leapman, R. D.; Rizzo, N. W.; Dyda, F.; Reed, J.; Tycko, R. *Biochemistry* **2000**, *39*, 13748–13759.
- (115) Rojas, A. V.; Liwo, A.; Scheraga, H. A. *J. Phys. Chem. B* **2011**, *115*, 12978–12983.
- (116) Liu, G.; Prabhakar, A.; Aucoin, D.; Simon, M.; Sparks, S.; Robbins, K. J.; Sheen, A.; Petty, S. A.; Lazo, N. D. *J. Am. Chem. Soc.* **2010**, *132*, 18223–18232.